Available online at www.sciencedirect.com
SCIENCE DIRECT®
Journal of Solid State Chemistry 177 (2004) 1000–1010
JOURNAL OF SOLID STATE CHEMISTRY
http://elsevier.com/locate/jssc

Synchrotron X-ray absorption of $LaCoO_3$ perovskite

O. Haas,[a,*] R.P.W.J. Struis,[a] and J.M. McBreen[b]

[a] *Paul Scherrer Institut, General Energy Research, CH-5232 Villigen PSI, Switzerland*
[b] *Brookhaven National Laboratory, Materials Science Department, Upton, NY 11973, USA*

Received 23 May 2003; received in revised form 1 September 2003; accepted 6 October 2003

Abstract

$LaCoO_3$ perovskite was prepared at 700°C using citrate precursors. The product was then characterized with X-ray diffraction (XRD) and X-ray absorption spectroscopy (XAS). The powder XRD pattern indicates rhombohedral ($R\bar{3}c$) or its monoclinic $I2/a$ subgroup symmetry. The electronic configuration and the short-range atomic structure of the $LaCoO_3$ perovskite at room temperature were investigated using synchrotron near-edge X-ray absorption spectroscopy (XANES) and extended X-ray absorption spectroscopy (EXAFS). From the XANES region of the XAS we conclude that Co(III) is at least partly in its intermediate- or high-spin state, which is in accordance with most of the published literature on $LaCoO_3$ perovskite. The EXAFS region of the $LaCoO_3$ perovskite spectrum, which up to now was almost not investigated, was simulated satisfactorily for the first two radial structure peaks in terms of the dominant scattering contributions generated with the FEFF8 code and the structural information available from crystallographic data. The best simulation results were obtained with $I2/a$ symmetry. The obtained amplitude reduction factor, zero-energy shift and Debye–Waller factors are useful reference values for data analyses of similar compounds like partly substituted $LaCoO_3$ perovskite, such as $La_{1-x}Ca_xCoO_3$ or $La_{1-x}Sr_xCoO_3$, which are materials of technical interest in catalyst and other applications.

Keywords: $LaCoO_3$; Electronic structure; X-ray absorption spectroscopy; FEFF8 simulation

1. Introduction

Cobalt oxides and, especially, perovskite structured cobaltates show interesting catalytic, oxygen ion-conducting, magnetic and semiconducting properties. $LaCoO_3$ shows catalytic activities, e.g., for the decomposition of NO_x, for the combustion of methane and propane, and for the oxidation of CO [1,2]. $La_{1-x}Ca_xCoO_3$ can be used as a catalyst in bi-functional porous oxygen diffusion electrodes to reduce oxygen to water and vice versa [3–6] whereas $La_{1-x}Sr_xCoO_3$ is widely used as an oxygen ion and electron conducting cathode material in high-temperature fuel cells [7,8]. $LaCoO_3$ is unique in that it is a diamagnetic semiconductor at very low temperatures [9]. It undergoes a spin-state transition at about 100 K leading from a diamagnetic to a paramagnetic state and above 500 K it changes from a semiconductor to a metal.

Synchrotron X-ray absorption spectroscopy (XAS) is a very useful tool to investigate the structural and electronic properties of these compounds. In many cases it offers even the possibility for in situ investigations and thus a tool to follow structural and electronic changes during an ongoing process. Information about the valence state of the cobalt and the electron configuration can be obtained from the near-edge X-ray absorption spectroscopy (XANES) region of the Co *K*- or *L*-edge absorption, whereas the extended X-ray absorption spectroscopy (EXAFS) region can be used to probe the local structure around the cobalt. The relevant structural parameters can be obtained if the background subtracted and normalized spectrum, or the Fourier transformed one, is fitted using the EXAFS formula [10] together with a plausible structural model and reasonable estimates of the relevant scattering parameters, such as amplitude reduction factor, zero-energy shift, etc. In general, similarly composed substances with known structures are used to achieve unambiguous structural information of the investigated substance. On the other hand, if the structure of the compound is well

*Corresponding author. Fax: +41-56-310-2199.
E-mail address: otto.haas@psi.ch (O. Haas).

0022-4596/$ - see front matter © 2003 Elsevier Inc. All rights reserved.
doi:10.1016/j.jssc.2003.10.004

known, as with $LaCoO_3$, ab initio calculations of the different scattering paths can be used to simulate the experimental spectrum and to fit the relevant scattering parameters. The obtained scattering parameters are very useful to evaluate the structure of similar compounds. We think that $LaCoO_3$ would be a good reference for the technically important $La_{1-x}Ca_xCoO_3$ or $La_{1-x}Sr_xCoO_3$ perovskites. For $LaCoO_3$, the rhombohedral perovskite phase was reported to be stable over a large range of oxygen partial pressures up to 1173 K [11,12]. Therefore, $LaCoO_3$ is an easily prepared reference material.

Numerous XRD and XANES investigations with $LaCoO_3$ and related compounds have been reported in the literature, but to our knowledge there is no systematic, in-depth, EXAFS investigation including curve fitting to evaluate the main scattering contributions and associated structural parameters. With this work we would like to close this gap and perform some simulations on $LaCoO_3$ Co K-edge EXAFS. Using the well-known crystal lattice parameters of $LaCoO_3$, particularly, coordination numbers (CN), interatomic distances (R) and location of atoms neighboring cobalt, it should be possible to obtain accurate parameter values for the amplitude reduction factor (S_0^2), the zero-energy shift (ΔE_0), and the Debye–Waller factor (σ^2), which are valuable reference values for XAS investigations of similar perovskite compounds.

2. Experimental procedures

$LaCoO_3$ perovskite was prepared using the citrate acid precursor method [4]. Stoichiometric amounts of $La(NO_3)_3 \cdot 6H_2O$ (Fluka) and $Co(NO_3)_2 \cdot 6H_2O$ (Fluka) were added to an aqueous 1 M citric acid solution. The solution was evaporated at 70°C using a rotary evaporator and the syrupy remainder dried for 3 days at 90°C. The resulting powder was heated in air for 2 h at 200°C and calcined in air for another 2 h at 700°C. The obtained product was a single phase, perovskite type oxide, as was verified by X-ray diffraction (XRD) using a Philips X-Pert Diffractometer with Cu $K\alpha$ radiation. The oxygen stoichiometry was verified using Cu^{1+}/Cu^{2+} coulometric titration as described by Karppinen et al. [13]. Within the error of the method no excess or vacancy of oxygen could be detected.

X-ray absorption measurements were carried out on beam line X-11A of the National Synchrotron Light Source, with the storage ring operating at 2.52 GeV beam energy and beam currents between 140 and 340 mA. A Si(111) double-crystal monochromator was used for energy selection. The monochromator was detuned by 20% to suppress higher harmonic radiation. The intensities of the incident and transmitted X-rays were monitored by nitrogen filled ionization chambers. The monochromator was scanned in energy from 200 eV below to 800 eV above the Co K absorption edge. The Co K-edge XAS of the $LaCoO_3$ sample and that of a 7 μm thin Co foil (for purpose of energy calibration) were measured simultaneously in transmission mode at room temperature. Reduction of the absorption data was performed with the software program WINXAS [14] using standard procedures, [15] which included energy calibration, background subtraction and normalization. The resulting $\chi(k)$ function was then weighted with k^3 to correct for dampening of oscillations with increasing k. The radial structure function was obtained by Fourier transformation of $k^3\chi(k)$. The WINXAS program was also used to fit the EXAFS regions using theoretical scattering paths, which we generated with the FEFF8 ab initio simulation code [16] and crystal lattice parameters known from literature.

3. Results and discussion

3.1. XRD results and structure of $LaCoO_3$

The XRD data (see Fig. 1) show the typical perovskite pattern expected for this compound [17–20]. The characterization of the $LaCoO_3$ structure started more than five decades ago, [21] and is still ongoing due to the much more sophisticated, high-resolution structural analysis tools. ($R\bar{3}c$) symmetry with $LaCoO_3$ powder at room temperature [22–24] has been accepted until very recently where Maris et al. [25] advocated the more refined $I2/a$ symmetry (more precisely $I12/a1$ with space group number ♯15 of the International Tables for Crystallography (ITC)). They analyzed single-crystal and powder samples of $LaCoO_3$ with high angular resolution neutron and XRD techniques for temperatures between 90 and 295 K. Their results revealed a further lowering in the symmetry from $R\bar{3}c$ (ITC ♯167) to its monoclinic subgroup, $I2/a$. Whereas $R\bar{3}c$ is characterized by one Co–O distance only, $I2/a$ symmetry allows further differentiation of the Co–O bond lengths. In particular, with $I2/a$ two oxygen positions describe the oxygen framework and three different Co–O distances result from this low symmetry space group. $I2/a$ symmetry does not generate new reflections compared to those already described with $R\bar{3}c$ in the region which we investigated with XRD, which means that we are not able to differentiate between $R\bar{3}c$ and $I2/a$ symmetry using our measured XRD pattern.

Fig. 1 shows the experimental XRD pattern of $LaCoO_3$ after subtraction of the baseline, which we reproduced satisfactorily well by assuming it to decay exponentially with increasing 2θ angle value. The resulting XRD pattern compares well with the X-ray data in the literature, apart from some deviations in the

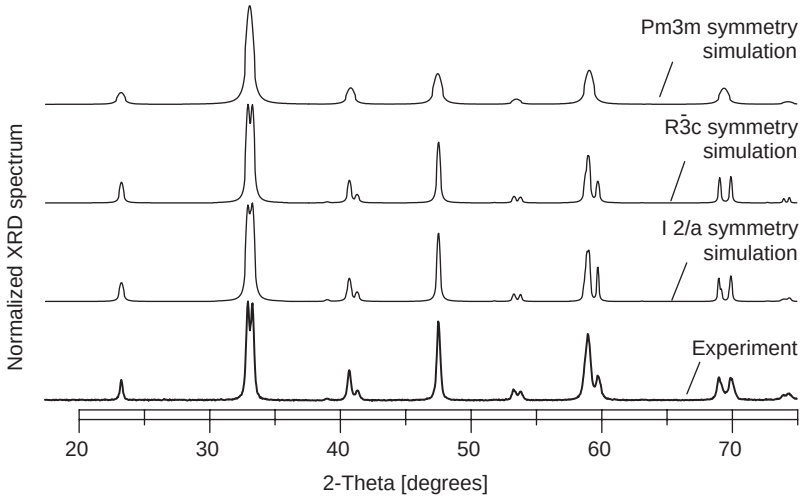

Fig. 1. Typical X-ray powder diffraction pattern of $LaCoO_3$ prepared at 700°C (experimental), together with simulated patterns assuming cubic (*Pm3m*) rhombohedral ($R\bar{3}c$), and monoclinic $I2/a$ space group symmetry.

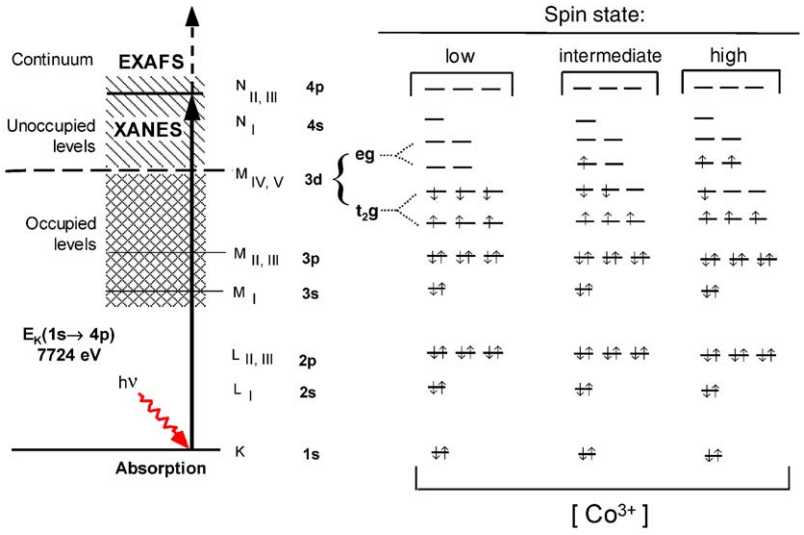

Fig. 2. Molecular orbital scheme of Co(III) and possible XAS transitions. The indicated $E_K(1s \rightarrow 4p)$ value of 7724 eV exemplifies the experimentally derived edge position of $LaCoO_3$ at room temperature.

intensities with certain reflections. Also shown with Fig. 1 are simulated XRD spectra for $LaCoO_3$ assuming *Pm3m*, $R\bar{3}c$ and $I2/a$ space group symmetry. For the simulations we used the program PowderCell (Window version 2.4) [26]. It shows that our diffraction pattern agrees well with $R\bar{3}c$ and $I2/a$ symmetry, whereas *Pm3m* symmetry (ITC ♯221) clearly provided inferior accordance, which is reasonable since the marked splitting of certain reflections, such as, e.g., the reflection at $2\theta = 33°$ is not expected with the cubic space group.

3.2. Electron configuration of $LaCoO_3$

The spin state and electron configuration of $LaCoO_3$ have been subject of numerous investigations and discussions over the past 30 years [12,27–35]. To facilitate the discussion, Fig. 2 shows the low-, intermediate- and high-spin electron configuration of Co(III) schematically, together with the main *K*-edge ($1s \rightarrow 4p$) and ($1s \rightarrow$ continuum) transitions, which in our energy calibrated XANES spectrum with $LaCoO_3$ shows the edge with the highest first derivative value at 7724.0 eV. Note that this scheme does not account for a possible band structure nor for Jahn–Teller splitting and ligand-to-metal charge transfer (LMCT) shake-down energy levels mentioned hereafter.

Octahedral oxygen coordinated Co(III) compounds normally have an undistorted cubic symmetry with a low-spin $\pi^*(t_2g^6)$ configuration ($^1A_1$), albeit that ligand-to-metal charge transfer processes may formally lead to configurations with seven electrons on the cobalt and a ligand hole ($t_2g^6 eg^1 \underline{L}^1$) as well. This is especially true for

strong covalent bonds between the cobalt and the ligands. As an exception to the normal case $LaCoO_3$ is either in an intermediate, $(^3T_1)t_2g^5eg^1$, or partially in a high-spin state, $(^5T_2)t_2g^4eg^2$. This supposition is supported by XRD studies showing that the low spin favored cubic (thus undistorted) structure is not rigorously maintained with this compound [22] and by susceptibility measurements revealing that $LaCoO_3$ has a low-spin configuration at very low temperatures only. Whereas there seems to be a general consensus that the crystal field splitting with $LaCoO_3$ is not large enough to produce a clean Co(III) t_2g^6 low-spin configuration at room temperature, the actual spin state is still under debate. As far as the high-spin configuration is concerned, we note that spin orbital interactions may split the high-spin state in slightly different energy levels, which may not be resolved well in our XANES experiments. The intermediate-spin configuration, $(^3T_1)t_2g^5eg^1$, may also be of some importance with $LaCoO_3$. In fact, the population of the intermediate $^3T_1$ state explains the observed temperature-dependent susceptibility best [36]. The susceptibility shows no clear low-to-high spin transition at a specific temperature as it increases gradually with temperature up to about 90 K and then passes through a maximum of about 1.7×10^{-5} emu/g [32]. It was therefore also argued that the eg and t_2g orbitals are not isolated states, but form electronic bands with a collective electron character of the $3d$ states, [28,30,32] where the electron population of the σ^* (eg) band is growing with increasing temperature at the expense of the $\pi^*(t_2g)$ band population. Recently, Ravindran et al. [37] underlined in a very profound discussion about the spin state and spin transitions of $LaCoO_3$ that the intermediate spin-state configuration is of much importance to understand the properties of $LaCoO_3$ and that at intermediate temperatures the low-to-intermediate spin-state transition is the more probable transition than the low-to-high spin transition.

The Co K-edge XANES spectrum with $LaCoO_3$ contains valuable information about the Co(III) electron configuration, but one has to be aware of the fact that the near-edge region may also contain multiple-scattering contributions, and that the core hole produced by the absorption process may alter the electron configuration to some extent. Moreover, the short-lived $1s^1$ core hole is broadening the bands and favors low-spin configuration. Different workers judge the impact of the core hole potential differently. For example, from the theoretical analysis of cobalt and oxygen K-edge XANES spectra, Wu et al. [38] concluded that the core hole potential effects are small and can be neglected at least in qualitative discussions of the electron configuration. Suzuki et al. [27], on the other hand, used the DV-Xα method to calculate the electronic structure of the ground state and they reached the conclusion that the $1s^1$ core hole changes the high-spin configuration to low spin. These calculations, however, suffer from the fact that they involved clusters which are too small to account for effects resulting, e.g., from delocalized electrons in a band structure.

3.3. Interpretation of the XANES spectrum

The raw XAS spectrum we obtained with $LaCoO_3$ powder is very much the same as the one published by Thornton et al. [39], except that their energy calibration seems to be off by about 10 eV. (Our energy scale was calibrated with a Co metal foil as reference using 7709 eV for the Co K-edge energy, which we assigned to the energy value, where the first derivative of the K-edge signal shows its highest value. The $RECoO_3$ spectra (RE= La, Y, Ho, Gd, Nd) measured by Thornton et al. were apparently not calibrated.) Prior to the XANES analysis, we applied a linear baseline correction to the absorption data in the early pre-edge range ($E = 7524-7670$ eV) and a five-knot spline to the after-edge range ($E\sim7726-8473$ V) to correct for the energy-dependent absorption baseline. The data were then normalized by setting a point located at about 800 eV above the edge to unity. The normalized data were analyzed in the XANES region between 7694 and 7728 eV. Deconvolution of this energy region renders three main components [40]: (1), a term describing the pre-edge background (or imperfections from the applied pre-edge correction), (2), a step function, STEP(E), due to electron transitions from the $1s$ state to the continuum, and, (3), Gaussian, Lorentzian, or Voigt profile functions to reproduce peak features due to the main and minor resonance transitions. Analyzing our data revealed that the transitions are represented best by Gaussian functions together with the integrated pseudo-Voigt (pV) function as the step function, i.e., $\mathrm{STEP}(E) = \int \mathrm{p}V(E)\,\mathrm{d}E = \eta_{\mathrm{STEP}}\mathrm{ARC}(E) + (1-\eta_{\mathrm{STEP}})\mathrm{ERF}(E)$ with η_{STEP} denoting the mixing parameter with values between 0 and 1, and p$V(E)$ the pseudo-Voigt approximation function as described by Thompson et al. [41]. The purpose of using STEP(E) instead of a full error function, ERF(E), is to describe the increase of the absorption in the early pre-edge range more accurately by the broader tail provided by the arc-tangent function, ARC(E). Both, ARC(E) and ERF(E), and thus also STEP(E), converge to unity for $E\to\infty$ (in our case 800 eV above the main edge) in compliance with the normalized absorption data. We fitted the corrected absorption data as well as their first, second, third, and fourth derivatives taken with respect to the X-ray energy simultaneously to raise the fitting accuracy. The description and justification of our fitting procedure are given in a forthcoming paper [42]. The experimental and fitted data for the normalized absorption spectrum and its second derivative are presented in Fig. 3, together with the fitted parameters (E^*, A, Γ)

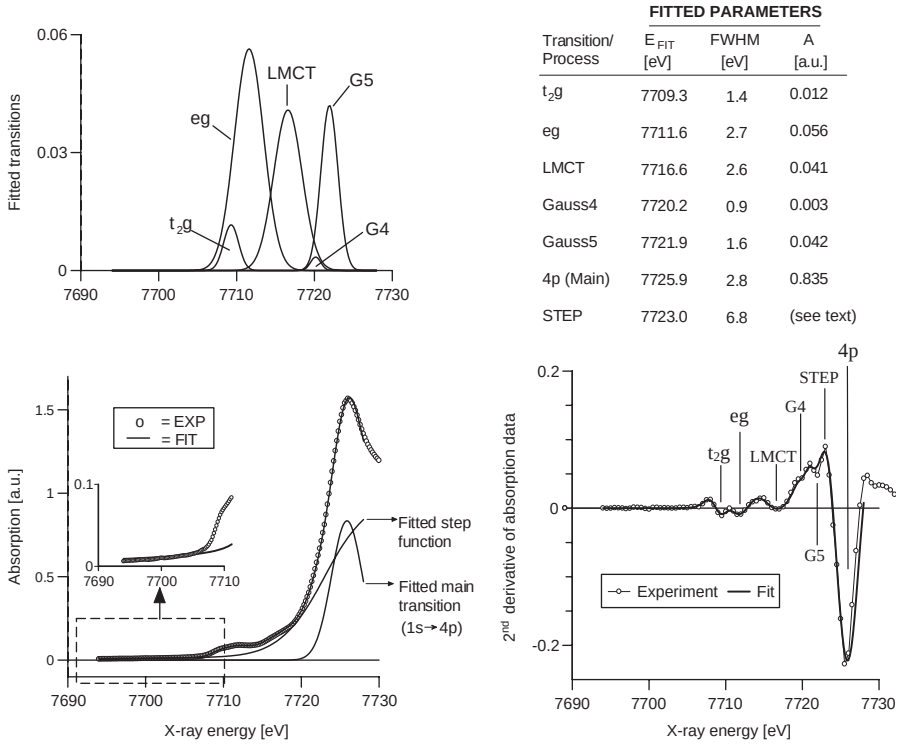

Fig. 3. (**Left**) Experimental (o) and fitted (—) results for the Co *K*-near edge absorption data of $LaCoO_3$. The plot at the top shows all fitted Gaussian-shaped pre-edge contributions. (**Right**) Experimental and fitted results for the second derivative of the absorption data, together with fitted parameter values (top) for the step function and the Gaussian-shaped pre-edge contributions.

pertaining to the Gaussian function, $G(E) = A\exp(-[(E-E^*)/\Gamma]^2)$, describing resonant transition pre-edge peaks, with A is denoting the dimensionless amplitude, E^* the position of the absorption maximum on the energy scale, and Γ the full-width at half-maximum of the absorption peak. The experimental absorption and all (first–fourth) derivative data could be reproduced very well over the entire investigated XANES energy range ($E = 7694-7728$ eV) and the step function (with $\eta_{STEP} = 0.25$ and $\Gamma_{STEP} = 6.8$ eV) allowed a good reproduction of the foot of the absorption spectrum (see inset on the lower, left-hand side plot of Fig. 3 showing an enlarged view of the early pre-edge region).

The dipole-allowed main transition ($1s\rightarrow 4p$) constitutes the largest feature of the second derivative curve shown in Fig. 3. The ($1s\rightarrow 4p$) transition maximum at 7725.9 eV was obtained by the deconvolution procedure discussed above and should not be confused with the inflection point in the Co *K*-edge leading to the largest value with the first derivative of the absorption data at 7724.0 eV. Since the Co *K*-edge is usually put on par with the $1s\rightarrow 4p$ transition it is questionable which is the right value to use, especially if this energy value is used to evaluate the valence state of Co.

The *d* orbitals of Co(III) mix heavily with the oxygen 2*p* orbitals [10] and the Co(III) t_2g and *eg* orbitals are expected to split by the crystal field and by the intra-atomic exchange energy (Hund's rule coupling) [43,44]. Although formally disallowed in the dipole approximation, a finite transition probability for the $1s\rightarrow t_2g$, respectively, $1s\rightarrow eg$ transition comes from oxygen *p* state mixing and the quadrupole transition [45]. In line with the above, we assigned the pre-edge features appearing in Fig. 3 below 7715 eV to Co(III) $1s\rightarrow 3d$ transitions. This pre-edge absorption is not very well resolved, but the second derivative data reveal still two features separated by 2.3 eV, which is probably due to the crystal field splitting of the t_2g and *eg* orbitals by the octahedral coordinated oxygen ligands. The fact that these pre-edge features are not clearly resolved may either indicate delocalized electrons in a band structure, or, an overlapping mixture of low- ($^1A_1$), intermediate- ($^3T_1$) and high-spin ($^5T_2$) states. The intra-atomic exchange energy is also splitting the t_2g and *eg* transitions, which may not be resolved well and appears as an additional broadening of these bands. The intra-atomic exchange energy splitting may be comparable in size as the crystal field splitting as recently proposed for the $LaCoO_3$ perovskite by Toulemonde et al. [44]. An additional small splitting is also expected from electron configurations, which lead to Jahn–Teller distortion.

We note that the second derivative of the absorption data with $DyCoO_3$ reported by Kim et al. [46] resemble

ours with $LaCoO_3$ to a large extent, except that our data revealed more details (see transitions "G4" and "G5" in Fig. 3), and that their energy positions for the $1s\rightarrow 3d$ transitions and the main transition ($1s\rightarrow 4p$) are all about 3.1($\pm$0.2) eV lower. We believe that the discrepancies in energy positions result from a different energy calibration. Unfortunately, Kim et al. gave no details on their energy calibration procedure apart from stating that copper metal and cobalt oxide (Co_2O_3) powder were used for calibration without specifying which feature was used to calibrate. Interestingly, and not dependent on the calibration procedure, is the fact that their analysis revealed almost the same energy splitting in the pre-edges. They assigned the first absorption bands to $1s\rightarrow t_2g$ and $1s\rightarrow eg$ transitions and attributed the observed spitting of about 2.3 eV to the crystal field splitting. Their energy difference between eg and $4p$ of about 14.7 eV is very close to our result with $LaCoO_3$ (14.3 eV). These similarities are also in line with the $RECoO_3$ spectra (RE= La, Y, Ho, Gd, Nd) at 300 K reported by Thornton et al. [39] They observed an energy splitting of about 2.2 eV for the $1s\rightarrow 3d$ transitions and about 15 eV between the $1s\rightarrow 3d$ and $1s\rightarrow 4p$ transitions, irrespective of the rare-earth cation.

The shoulder at about 7716.6 eV is most probably due to the ($1s\rightarrow 4p$) main transition followed by a LMCT shake-down process, viz., $1s^1\underline{c}3d^6\underline{L}^2\rightarrow 1s^1\underline{c}3d^7\underline{L}^1$; with $\underline{c}$ = core hole and $\underline{L}$ = ligand hole, as advocated by Kim et al. [46] in the paper about $Dy_{1-x}Ca_xCoO_3$ or by Chainani et al. [47] for $Ca_{1-x}Sr_xCoO_3$. The latter authors estimated that this LMCT state contributes about 45% to the core hole ground state, and they estimated that this ground state should even contain about 14.5% of $1s^1\underline{c}3d^8\underline{L}^2$.

With respect to the pre-edge transitions labelled t_2g, eg, "G4", and "G5" in Fig. 3, we would like to refer to complementary information from oxygen K-edge measurements with $LaCoO_3$. Toulemonde et al. [44] ascribe in their oxygen K-edge spectrum at 300 K a band at about 531 eV to the $O(1s)\rightarrow Co(3d)-O(2p)$ hybrid transition, which is split in three parts. The splitting was attributed to crystal field and the spin up ($\uparrow$) and down ($\downarrow$) splitting (intra-atomic exchange energy). The spin splitting can be estimated to be about 1 eV (531.7−530.7 eV) and the $t_2g\uparrow$ an $eg\uparrow$ splitting (assuming intermediate-spin state) about 2.3 eV (531.7−529.4 eV). At about 14 eV higher energy, another band was assigned to the $O(1s)\rightarrow Co(4sp)-O(2p)$ hybrid transition. The band shows two maxima split by about 2 eV. Although the intensities of these bands are different in our Co K-edge XANES (which is probably due to different transition probabilities), they have many energy features in common with our pre-edge absorption bands. The assignment of the $O(1s)\rightarrow Co(4sp)-O(2p)$ hybrid transitions between 540 and 550 eV correspond well with our "G4" and "G5" contributions at 7720.2 and 7721.9 eV, and G4 and G5 may therefore be assigned to $Co(1s)\rightarrow Co(4sp)$ hybrid transitions.

Assuming that the crystal field splitting is larger than the spin splitting, we conclude that the pure low-spin configuration with $LaCoO_3$ at room temperature can be excluded due to the fact that we observe more than only the $1s\rightarrow eg$ transition (which would indicate low-spin configuration only) as early pre-edge features.

3.4. Interpretation of the EXAFS region

The only analyses of the EXAFS region we are aware of were published by Akunarkavalli et al. [49] and Colonna et al. [49] Akunarkavalli et al. reported first EXAFS investigations on $LaCoO_3$ at different temperatures using a Rigaku spectrometer attached to a rotating anode X-ray generator. Using structural information from $CoAl_2O_4$ as a reference, they deduced a single Co–O distance with all six oxygen ligands at room temperature. At higher temperatures they found two Co–O distances, each corresponding to three oxygen ligands, together with additional features at about twice the Co–O distance, which they attributed to Co–La and Co–Co distances. Their findings at room temperature resemble ours, except that our radial structure function shows an inverse intensity ratio for the first two peaks. Colonna et al. studied $LaCoO_3$ perovskites on ZrO_2 support. They used Co_3O_4 as reference compound and fitted the Fourier-transformed EXAFS spectra of $LaCoO_3$ using the standard EXAFS formula together with crystallographic data, leaving as variable the E_0 shift, the S_0^2 term and the Debye–Waller factors (unfortunately without reporting the fitted E_0 shift and S_0^2 values). To our knowledge a detailed analysis of the first peak appearing in the radial structure function in terms of scattering paths generated with the FEFF8 code [14,50] has not been published yet and the other peaks of the radial structure function have not been analyzed at all. We think it is well worthwhile to make this effort. The thus obtained characteristic parameters might serve as valuable reference values for cobalt oxides with similar structures in the future. Using reference substances has become a frequently used method to obtain reliable structural parameters from EXAFS spectra [51]. The knowledge about the electronic and atomic structure of the chemically very stable, single-phase $LaCoO_3$ makes this substance an interesting reference compound.

Fig. 4 shows the radial structure function as a function of the (phase-uncorrected) interatomic distance, R(Å), which we obtained by Fourier transformation of $k^3\chi(k)$ over the k-space range between 4.5 and 12.0 Å^{-1}, thus we employed absorption data between $(E-E_0)\sim 75$ and 540 eV, using a Bessel function envelope with the WINXAS software-defined Bessel

window parameter value of four to diminish artifacts due to the finite Fourier filtering range. From Fig. 4 it can be recognized that with $LaCoO_3$ at room temperature the radial structure function reveals two strong peaks at lower, and two weaker ones at higher distances.

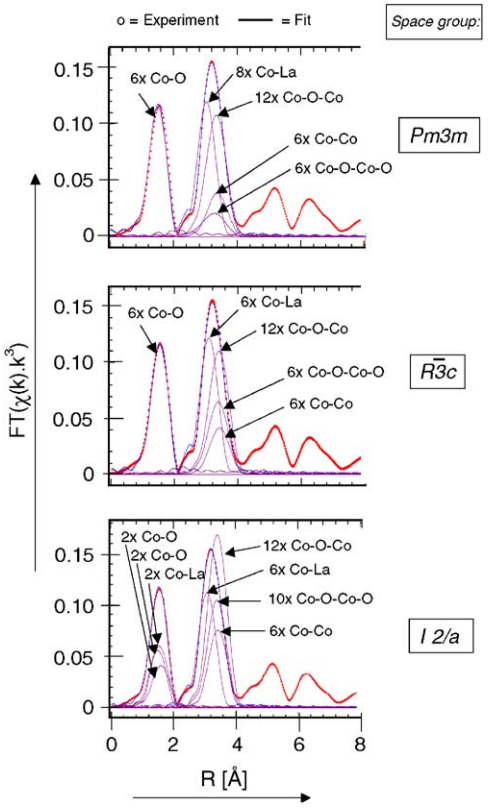

Fig. 4. Experimental (o) and fitted (—) radial structure function data as a function of the phase-uncorrected distance, R [Å], using *Pm3m* $R\bar{3}c$, and $I2/a$ space group symmetry. The fitted parameter values are given in Table 3.

With respect to Akunarkavalli et al. [48], we note that their RSF data show a stronger first peak. Their RSF was based on absorption data between $(E-E_0)\sim 30$ and 520 eV, whereas we used data between $(E-E_0)\sim 75$ and 540 eV. Therefore, the first peak in their RSF might indeed be larger as a result of more important multi-scattering contributions in the near-edge absorption range.

Amplitude and phase corrections are necessary to obtain the correct radius of the shells. This can be done using experimental spectra from reference samples with similar atomic structures or by fitting the experimental $k^3\chi(k)$ or the related radial structure function using theoretical scattering functions pertaining to the supposed atomic structure of the sample. Since the structure of $LaCoO_3$ at room temperature is well known from crystallographic data, we used the latter possibility. In particular, we employed three different space group symmetries reported in the literature for $LaCoO_3$: the simplified cubic *Pm3m* symmetry with the structural parameters (see Table 1a) reported by Wold and Ward [17], the more refined rhombohedral $R\bar{3}c$ symmetry with the structural parameters (Table 1b) evaluated by Thornton et al. [23], and the most-recently reported monoclinic $I/2a$ symmetry by Maris et al. [25] with the structural parameters given in Table 1c. The aim of this EXAFS analyses was to elucidate which symmetry fits best to our EXAFS data and to evaluate the characteristic EXAFS parameters.

3.5. EXAFS analyses

Quantitative analyses were performed with the first two peaks appearing in the radial structure function between $R=0.9$ and 4.2 Å (see Fig. 4) by fitting them to a set of theoretical scattering paths pertaining to the

Table 1
Atomic positions of $LaCoO_3$ in the unit cell

Atom	M	(Wy)	X	Y	Z
(a) *At room temperature based on Pm3m (ITC #221) space group symmetry with unit cell lengths* $a=b=c=3.82$ *Å and angles* $\alpha=\beta=\gamma=90°$					
La	1	(*a*)	0.0	0.0	0.0
Co	1	(*b*)	0.5	0.5	0.5
O	3	(*c*)	0.5	0.5	0.0
(b) *At* $T=293$ *K based on* $R\bar{3}c$ *(ITC #167) space group symmetry with unit cell lengths* $a=b=c=5.3778$ *Å and angles* $\alpha=\beta=\gamma=60.798°$					
La	2	(*a*)	0.25	0.25	0.25
Co	2	(*b*)	0.00	0.00	0.00
O	6	(*e*)	0.1982	0.3018	0.75
(c) *At 200 K based on I2/a (ITC #15) space group symmetry with unit cell lengths* $a=5.3611$ *Å,* $b=5.4316$ *Å,* $c=7.6318$ *Å and angles* $\beta=91.056°$ *and* $\alpha=\gamma=90°$					
La	4	(*e*)	0.25	0.25019	0.00
Co	4	(*c*)	0.75	0.25	0.25
O1	4	(*e*)	0.25	−0.3068	0.00
O2	8	(*f*)	0.0241	0.0332	0.2293

M = Multiplicity; Wy = Wyckoff notation.

Table 2
Scattering paths, coordination numbers (CN), interatomic distances (R, Å) and curved-wave amplitude importance ratio (CW ratio, %) for the first two coordination shells generated with the FEFF8 code and the structural data for space group $Pm3m$, $R\bar{3}c$, respectively, $I2/a$

$Pm3m$ (♯221)				$R\bar{3}c$ (♯167)				$I2/a$ (♯15)[a]			
Path	CN	R	CW	Path	CN	R	CW	Path	CN	R	CW
Co–O	**6**	**1.910**	**100**	**Co–O**	**6**	**1.932**	**100**	**Co–O**	**2**	**1.874**[b]	**35**
Co–O–O	24	3.261	16	**Co–La**	**2**	**3.273**	**16**	**Co–O**	**2**	**1.925**[b]	**33**
Co–La	**8**	**3.308**	**62**	Co–O–O	12	3.283	8	**Co–O**	**2**	**1.993**[b]	**32**
Co–Co	**6**	**3.820**	**21**	Co–O–O	12	3.313	8	Co–La	2	3.262	16
Co–O–O	6	3.820	16	**Co–La**	**6**	**3.326**	**47**	Co–O–O	$\Sigma=20$	3.263–3.301	$\Sigma=14$
Co–O–Co	**12**	**3.820**	**57**	**Co–Co**	**6**	**3.826**	**21**	**Co–La**	**$\Sigma=6$**	**3.318–3.320**	**$\Sigma=46$**
Co–O–Co–O	**6**	**3.820**	**39**	**Co–O–Co**	**12**	**3.845**	**47**	Co–O–O	$\Sigma=6$	3.363–3.784	$\Sigma=8$
Co–O–Co–O	6	3.820	13	Co–O–La	12	3.855	6	Co–O–Co–O	4	3.784	7
Co–O–Co–O	6	3.820	6	Co–O–O	6	3.864	16	**Co–Co**	**6**	**3.816**	**22**
Co–O–Co–O	24	3.820	<3	**Co–O–Co–O**	**6**	**3.864**	**28**	Co–O–La	$\Sigma=8$	3.829–3.830	$\Sigma=4$
Co–O–La	48	3.960	17	Co–O–Co–O	6	3.864	12	**Co–O–Co**	**$\Sigma=12$**	**3.835–3.841**	**$\Sigma=47$**
				Co–O–Co–O	6	3.864	6	**Co–O–Co–O**	**$\Sigma=10$**	**3.854–3.866**	**$\Sigma=33$**
								Co–O–O	$\Sigma=4$	3.866–3.925	$\Sigma=11$
								Co–O–La	4	3.866	2
								Co–O–Co–O	4	3.925	6

More important paths are printed in bold.

[a] To facilitate the comparison between the three space groups, the CW ratio values of the $I2/a$ space group were renormalized such that the sum of the CW values for the first three Co–O paths equals 100%. With the second Co shell, we combined neighboring scattering paths of the same type into one effective path with CN and CW equal to the sum given by the individual paths (indicated by "$\Sigma=$").

[b] First shell Co–O distances pertaining to $LaCoO_3$ at 298 K (see text).

three different lattice symmetries, i.e., $Pm3m$, $R\bar{3}c$, and $I/2a$, respectively. Each set was generated with the ab initio self-consistent real space multiple-scattering code FEFF8 [16], using the program ATOMS (version 3) [52] to create the input file for FEFF8 on the basis of the atomic and unit cell parameters given in Table 1a-c. Table 2 summarizes the generated scattering paths up to a radius of about 4 Å, where each backscattering path is specified together with the expected CN (or more precisely, multiplicity or degeneracy of the paths), interatomic distance (R), and the *relative* weight of each path in terms of the curved-wave amplitude importance ratio (CW in %). Table 2 shows different multi-scattering paths for the same atom combinations as a result of the different angles involved. With the $I2/a$ space group symmetry, we recombined the more important multi-scattering paths (printed in bold) into one effective path in case that the angles and path distances are almost identical. With FEFF8, CW is estimated from curved-wave MS calculations [53] assuming the same Debye–Waller factor (here $\sigma^2 = 0$) for all paths. The CW value comprises the multiplicity of the path and the scattering properties of the atoms involved. In practice, however, σ^2 is path dependent and tends to increase with shell distance and complexity of the scattering path. But, a pre-selection of the dominant scattering paths on the basis of the CW value is very helpful, particularly, when comparing the impact of different paths within one scattering shell. The more important scattering paths are printed in bold with Table 2. Including other paths proved to be irrelevant to the quality of the fits. From Table 2 it follows that the first peak in Fig. 4 corresponds to the first Co–O coordination shell only, whereas the second peak comprises single and multi-scattering contributions. As the number and complexity of the generated paths rises drastically with distance, we restricted the experimental fitting range only to the first two radial structure function peaks within the distance interval between 0.9 and 4.15 Å.

With WINXAS, each path can be adjusted in terms of five parameters, i.e., amplitude reduction factor (S_0^2), CN, interatomic distance (R), Debye–Waller factor (σ^2), and the zero-energy shift parameter (ΔE_0). The value of ΔE_0 depends on the starting energy of the EXAFS spectrum and the charge transfer properties of the atoms in the backscattering shells. ΔE_0 is given here with respect to E_0, the Co K-edge energy of the perovskite (7724.0 eV). When fitting the experimentally derived radial structure function to more than one scattering path, ΔE_0 can be varied with each path separately; however, it is a dangerous parameter to fit since it affects the position, intensity and width of the peaks in each theoretical path. In practice, this means that almost everything can be fitted if this parameter is not restricted to some limits. Therefore, some groups [54] prefer a single ΔE_0 value with all scattering paths. With $LaCoO_3$, we expect that the oxygen ligands (O^{2-}) transfer more charge to the central cobalt atom than, e.g., Co^{3+} or La^{3+} do, thus more negative ΔE_0 values would be expected from oxygen than from cobalt or lanthanum backscattering shells. Since the charge transfer to the central cobalt atom also strongly depends on the distance, the charge transfer from the second shell

should be less important. However, the FEFF8 code accounts for local charge transfer using self-consistent field calculations. Assuming that these calculations account correctly for the charge transfer properties of the different coordination shells, ΔE_0 should have the same value for all scattering paths.

The first peak between $R = 0.90$ and 2.12 Å in Fig. 4 can be reproduced reasonably well using the published crystallographic data with CN = 6 and $R = 1.93$ Å, thus adopting the structural results from the $R\bar{3}c$ lattice symmetry, or $R = 1.91$ Å (assuming $Pm3m$ symmetry), and even better if we assume three Co–O distances with $R = 1.892$, 1.9327, and 1.9623 Å pertaining to the $I2/a$ lattice symmetry for $LaCoO_3$ at 295 K [25].

Preliminary fits showed that S_0^2 was always close to 1, which is the expected value for S_0^2 if the FEFF8 code is used. For the following fits we therefore fixed this parameter to unity. Table 3 shows that the fitting residual decreases clearly as the symmetry of the space group decreases. The residual obtained assuming $I2/a$ or $R\bar{3}c$ symmetry is about four times better than with cubic $Pm3m$ symmetry. In addition, the ΔE_0 values for the $I2/a$ and $R\bar{3}c$ symmetry are also more reasonable than that with $Pm3m$ symmetry (−3.3 eV for $Pm3m$, +2.2 eV for $R\bar{3}c$, respectively, +1.0 eV for $I2/a$), as we expect ΔE_0 to be close to zero with our E_0 value. Additional support for $I2/a$ symmetry is also coming from the fact that the σ^2 values obtained for the three Co–O distances in $I2/a$ symmetry are lower than with the one Co–O distance expected for the other two symmetries. The quality of the fit is reflected in the fact that all three Co–O distances have very similar σ^2 values and, by the same token, led to similar area values (see Table 3) being also well in line with the CW ratio values provided by FEFF8 (see Table 2). We therefore conclude that the EXAFS analysis favors the $I2/a$ symmetry for $LaCoO_3$ at room temperature.

Additional structural information can be elucidated if the second peak of the RSF (which is due to scattering paths Co–La, Co–Co and multiple-scattering paths like Co–O–Co or Co–O–La, etc.) is included in the fit, thus fitting over the range between 0.90 and 4.15 Å. Reasonable fit results could be obtained if all single scattering paths (Co–O, Co–La, Co–Co) and at least two multi-scattering paths (Co–O–Co and Co–O–Co–O) were used. In these fits the CN and path distances were kept fixed to those given in Table 1a-c, and with the $I2/a$ space group symmetry we used the (CN weighted) average distance in case that neighboring paths of the same type were represented by one path effectively. The inclusion of Co–O–La or Co–O–O multi-scattering paths or that of the two-fold degenerated Co–La path with the non-cubic ($R\bar{3}c$ or $I2/a$) symmetries appeared of minor importance. All fitted parameters are listed in Table 3. It must be noted that the $I2/a$ fit for $T = 295$ K essentially uses the generated scattering paths pertaining to the structural analysis of Maris et al. for $LaCoO_3$ at 200 K except that we replaced the distances for the first three (Co–O) paths by those derived by Maris et al. for $T = 295$ K. As with the first peak analysis, the fitting

Table 3
Structural parameters for $LaCoO_3$ derived from the Co K-edge EXAFS analysis, respectively, assuming $Pm3m$, $R\bar{3}c$, and $I2/a$ space group symmetry: zero-energy shifts (ΔE_0, eV), residuals (%), and Debye–Waller factors (σ^2, Å$^2 \times 10^{-3}$)

	Space group								
	$Pm3m$ (♯221)			$R\bar{3}c$ (♯167)			$I2/a$ (♯15)		
	CN: path	σ^2	Area	CN: path	σ^2	Area	CN: path	σ^2	Area
First shell fit	6: Co–O	4.4	100	6: Co–O	4.6	100	2: Co–O	2.3	34
							2: Co–O	1.7	36
							2: Co–O	2.4	30
ΔE_0	−3.3 eV			+2.2 eV			+1.0 eV		
Residual[a] (%)	7.8			2.0			2.0		
First and second shell fit									
First shell	6: Co–O	4.4	97	6: Co–O	4.6	94	2: Co–O	2.3	32
							2: Co–O	1.3	34
							2: Co–O	3.4	24
Second shell	8: Co–La	7.4	62	6: Co–La	5.5	47	6: Co–La	6.0	68
	6: Co–Co	10	20	6: Co–Co	10	16	6: Co–Co	5.8	44
	12: Co–O–Co	12	59	12: Co–O–Co	9.1	43	12: Co–O–Co	6.0	100
	6: Co–O–Co–O	21	14	6: Co–O–Co–O	9.2	25	10: Co–O–Co–O	5.4	62
ΔE_0	−5.3 eV			+1.0 eV			−1.0 eV		
Residual[a] (%)	8.1			5.7			4.9		

The area value is calculated by the WINXAS software and constitutes the surface under each fitted path on a relative (%) scale.

[a] Residual indicates the deviation between experimental data and fit in percentage. With N representing the number of data points, and y_{exp} and y_{theor} the experimental and theoretical data points, Residual = $100\% \times \{[\Sigma_{i=1\ldots N}|y_{exp}(i)-y_{theor}(i)|]/\Sigma_{i=1,\ldots,N}|y_{exp}(i)|\}$.

quality improved going from $Pm3m$ (residual = 8.1%) via $R\bar{3}c$ (5.7%) to $I2/a$ symmetry (4.9%) and with $|\Delta E_0|$ values becoming systematically smaller, i.e., from 5.3 eV with $Pm3m$ to 1.0 eV with $I2/a$ and $R\bar{3}c$.

The problem with the fit of the second peak in the RSF is the fact that even if only the most important scattering paths are used there are still too many free parameters to be fitted, especially, when the symmetry is lowered. Thus from the second RSF peak the quality of the obtained information is not as good as with the first RSF peak where the free parameters were not as numerous. The only valuable hint in favor of $I2/a$ symmetry is the lower residual value obtained.

4. Conclusions

Summarizing all results, we conclude from the XANES region of the XAS spectrum that $LaCoO_3$ is at least not in the low-spin state only. The XANES data fit best to the intermediate state with a crystal field splitting of about 2.3 eV and an intra-atomic exchange energy of about 1 eV. The intermediate state is probably mixed with the low-spin state. It would be interesting to see if site selective XAS investigations could help to separate the spin states [55]. The EXAFS region shows two strong peaks for the first two atom shells and two weaker ones at higher distances. Whereas the first RSF peak (around 1.92 Å) depicts single (Co–O) scattering contributions, the second peak (with maximum around 3.3 Å) mainly contains contributions from single (Co–La, Co–Co) and multiple (Co–O–Co, Co–O–Co–O) scattering paths. Using the program WINXAS with the FEFF8 ab initio code option, we were able to simulate the first two RSF peaks reasonably well with both, $R\bar{3}c$ and $I2/a$ symmetry, whereas the $Pm3m$ symmetry was clearly the least satisfying and the $I2/a$ symmetry the best. This is especially evident when fitting the first RSF peak only.

Acknowledgments

Financial support of the Swiss Federal Office of Energy and the US Department of Energy is gratefully acknowledged. We also appreciated helpful discussions with Dr. D. Grolimund (PSI) and Dr. G. George (SSRL), and we thank A. Frei (PSI) for measuring the XRD data.

References

[1] R.J.H. Voorhoeve, D.W. Johnson Jr., J.P. Remeike, P.K. Gallagher, Science 195 (1977) 827.
[2] S. Colonna, S. De Rossi, M. Faticanti, I. Pettiti, P. Porta, J. Mol. Catal. A: Chem. 180 (2002) 161.
[3] D.B. Meadowcroft, Nature (London) 226 (1970) 847–848.
[4] Y. Shimizu, K. Uemura, H. Matsuda, N. Miura, N. Yamazoe, J. Electrochem. Soc. 137 (1990) 3430.
[5] S. Müller, K. Striebel, O. Haas, Electrochim. Acta 39 (1994) 1661–1668.
[6] O. Haas, F. Holzer, S. Müller, J.M. McBreen, X.Q. Yang, X. Sun, M. Balasubramanian, Electrochim. Acta 47 (2002) 3211–3217.
[7] C.S. Tedmon Jr., H.S. Spacil, S.P. Mitoff, J. Electrochem. Soc. 116 (1969) 1170–1175.
[8] K. Huang, H.Y. Lee, J.B. Goodenough, J. Electrochem. Soc. 145 (1998) 3220–3227.
[9] S. Yamaguchi, Y. Okimoto, H. Taniguchi, Y. Tokura, Phys. Rev. B 53 (1996) R2926–R2929.
[10] D.C. Koningsberger, R. Prins (Eds.), X-ray Absorption, Principles, Applications, Techniques of EXAFS, SEXAFS and XANES, Wiley, New York, 1988, p. 11 (Chapter 1).
[11] T. Nakamura, G. Petzow, L.J. Gauckler, Mater. Res. Bull. 14 (1979) 649–659.
[12] M.A. Senaris-Rodriguez, J.B. Goodenough, J. Solid State Chem. 116 (1995) 224–231.
[13] M. Karppinen, M. Matvejeff, K. Salomäki, H. Yamauchi, J. Mater. Chem. 12 (2002) 1761–1764.
[14] T. Ressler, J. Synchrotron Radiat. 5 (1998) 118–122.
[15] J.J. Rehr, R.C. Albers, S.I. Zabinsky, Phys. Rev. Lett. 69 (1992) 3397.
[16] A.L. Ankudinov, B. Ravel, J.J. Rehr, S.D. Conradson, Phys. Rev. B 54 (1998) 7565.
[17] A. Wold, R. Ward, J. Am. Chem. Soc. 76 (1954) 1029–1030.
[18] JCPDS-ICDD database, Card No. 84-0848, 1998.
[19] JCPDS-ICDD database, Card No. 75-0279, 1998.
[20] A. Wold, B. Post, E. Banks, J. Am. Chem. Soc. 79 (1957) 6365.
[21] F. Askham, I. Fankuchen, R. Ward, J. Am. Chem. Soc. 72 (1950) 6365.
[22] P.M. Raccah, J.B. Goodenough, Phys. Rev. 155 (1967) 932–943.
[23] G. Thornton, B.C. Tofield, A.W. Hewat, J. Solid State Chem. 61 (1986) 301–307.
[24] N.M.L.N.P. Closset, R.H.E. van Doorn, H. Kruidhof, J. Boeijsma, Powder Diffr. 11 (1996) 3.
[25] G. Maris, Y. Ren, V. Volotchaev, C. Zobel, T. Lorenz, T.T.M. Palstra, Phys. Rev. B 67 (2003) 224423.
[26] W. Kraus, G. Nolze, J. Appl. Cryst. 29 (1996) 301–303 http://users.omskreg.ru/~kolosov/bam/a_v/v_1/powder/e_cell.htm.
[27] Ch. Suzuki, J. Kawai, J-Y. Tanizawa, H. Adachi, S. Kawasaki, M. Takano, T. Mukoyama, Chem. Phys. 241 (1999) 17–27.
[28] H. Takahashi, F. Munakata, M. Yamanaka, Phys. Rev. B 53 (1996) 3731–3739.
[29] D.J. Lam, B.W. Veal, D.E. Ellis, Phys Rev. B 22 (1980) 5730–5739.
[30] G. Thornton, F.C. Morrisson, S. Partington, B.C. Tofield, D.E. Williams, J. Phys. C 21 (1988) 2871–2880.
[31] B.W. Veal, D.J. Lam, J. Appl. Phys. 49 (1978) 1461–1462.
[32] T. Saitoh, T. Mizokawa, A. Fujimori, M. Abbate, Y. Takeda, M. Takano, Phys. Rev. B 55 (1997) 4257.
[33] J.B. Goodenough, Mater. Res. Bull. 6 (1971) 967–976.
[34] M. Abbate, J.C. Fuggle, A. Fujimori, L.H. Tjeng, C.T. Chen, R. Potze, G.A. Saawatzky, H. Eisaki, S. Uchiada, Phys. Rev. B 47 (1993) 16124–16130.
[35] M. Pouchard, A. Villesuzanne, J.-P. Doumerec, J. Solid State Chem. 162 (2001) 282–292.
[36] M.A. Korotin, S.Yu. Ezhov, I.V. Solovyev, V.I. Anisimov, D.I. Khomskii, G.A. Sawatzky, Phys. Rev. B 54 (1996) 5309–5316.

[37] P. Ravindran, H. Fjellvåg, A. Kjekshus, P. Blaha, K. Schwarz, J. Luitz, J. Appl. Phys. 91 (2002) 291–303.
[38] Z.Y. Wu, M. Benfatto, M. Pedio, R. Cimino, S. Mobilio, S.R. Barman, K. Maiti, D.D. Sarma, Phys. Rev. B 56 (1997) 2228–2233.
[39] G. Thornton, I.W. Owen, G.P. Diakun, J. Phys. Condens. Matter 3 (1991) 417–422.
[40] A. Filipponi, J. Phys. B 33 (2000) 2835–2846.
[41] P. Thompson, D.E. Cox, J.B. Hastings, J. Appl. Cryst. 20 (1987) 79–83.
[42] R.P.W.J. Struis, in preparation.
[43] C. Zobel, M. Kriener, D. Bruns, J. Baier, M. Grüninger, T. Lorenz, Phys. Rev. B 66 (2002) 020402.
[44] O. Toulemonde, N. N'Guyen, F. Studer, J. Solid State Chem. 158 (2001) 208–217.
[45] A. Bianconi, Phys. Rev. B 26 (1982) 2741.
[46] M.G. Kim, Y.S. Im, E.J. Oh, K.H. Kim, C.H. Yo, Physica B 229 (1997) 338–346.
[47] A. Chainani, M. Mathew, D.D. Sarma, Phys. Rev. B 46 (1992) 9976–9983.
[48] T. Akunarkavalli, G.U. Kulkarni, C.N.R. Rao, J. Solid State Chem. 107 (1993) 299–301.
[49] S. Colonna, S. De Rossi, M. Faticanti, I. Pettiti, P. Porta, J. Mol. Catal. A: Chem. 180 (2002) 161–168.
[50] B. Ravel, http://feff.phys.washington.edu, 2001.
[51] C. Koningsberger, R. Prins (Eds.), X-ray Absorption, Principles, Applications, Techniques of EXAFS, SEXAFS and XANES, Wiley, New York, 1988, ISBN 0-471-87547-3.
[52] B. Ravel, J. Synchrotron Radiat. 8 (2001) 314–316.
[53] J.J. Rehr, A. Ankudinov, S.I. Zabinsky, Catal. Today 39 (1998) 263–269.
[54] M. Balasubramian, X. Sun, X.Q. Yang, J.M. McBreen, J. Electrochem. Soc. 147 (2000) 2903.
[55] P. Glatzel, L. Jacquamet, U. Bergmann, F.M.F. de Groot, St.P. Cramer, Inorg. Chem. 41 (2002) 3121.